AIMS Mathematics, 11(5): 13216–13232.
DOI: 10.3934/math.2026545
Received: 03 April 2026
Revised: 24 April 2026
Accepted: 29 April 2026
Published: 12 May 2026

https://www.aimspress.com/journal/Math

Research article

Bistability and delay-induced oscillations in a density-gated synNotch model

Huichao Xing[1], **Jun Wu**[1] **and Conghua Wang**[2,*]

[1] Faculty of Education, Yunnan Normal University, Kunming, Yunnan 650500, China

[2] Chongqing Municipal University Key Laboratory of Optimization Techniques and Intelligent Vehicle, National Center for Applied Mathematics in Chongqing, Chongqing Normal University, Chongqing 401331, China

* **Correspondence:** Email: chwang@cqnu.edu.cn.

Abstract: Synthetic signaling circuits provide a versatile framework for programming contact-dependent cell behaviors, yet their collective dynamics are strongly shaped by cell density and processing delay. In this work, we studied a reduced delay differential model motivated by synNotch-type signaling with density-dependent attenuation and adaptive inhibition. The analysis was organized along two complementary routes. First, the equilibrium structure was characterized through a density-driven saddle-node bifurcation analysis, which identified the emergence of a three-equilibrium region and, when the outer-branch trace condition is satisfied, a low/high bistable subinterval. Second, the local dynamics around positive equilibria were examined through a delay-induced Hopf bifurcation analysis, which determined the onset of oscillatory behavior and the associated stability switching. Numerical simulations confirmed the predicted branch structure and the delay-dependent stability switching on the upper equilibrium branch. These results provided a compact dynamical description of how density and intracellular processing time jointly regulated state selection and rhythmic activity in contact-mediated synthetic signaling systems.

Keywords: synNotch relay; delay differential equations; saddle-node bifurcation; Hopf bifurcation
Mathematics Subject Classification: 34K18, 34K20, 92C42

1. Introduction

Synthetic developmental systems seek programmable rules for multicellular organization [1–3]. Among the available platforms, synNotch receptors are especially useful because they convert contact-dependent recognition into user-defined transcriptional responses and thereby enable modular cell–cell communication in engineered tissues and therapeutic circuits [4–6]. In parallel, studies of endogenous Notch signaling have shown that contact geometry, ligand interactions, and force-

dependent activation shape signaling strength, temporal response, and spatial patterning [7–10]. This biophysical background makes synNotch systems a natural setting for quantitative dynamical analysis.

Recent experiments have clarified the importance of tissue context in synthetic juxtacrine signaling [11–13]. Santorelli et al. showed that cell growth and local density reshape the speed, spatial range, and temporal profile of synNotch signal propagation in multicellular relay circuits [14]. Dawson et al. further demonstrated that contact area and tissue growth dynamics influence synthetic juxtacrine activation patterns in vivo [15]. Related engineering studies have shown that synNotch outputs can also be spatially programmed through designed material interfaces and multicellular architectures [16]. These studies identify density, contact geometry, and response timing as primary determinants of collective synNotch behavior.

The spatial simulation framework in [14] incorporates weighted cell–cell contact, delayed ligand induction, cis-inhibition, and density-dependent attenuation, and it captures signal propagation in large lattices. However, that framework does not directly provide local conditions for state switching, bistability, or oscillatory onset [17–20]. Reduced analytical models are valuable in this setting because they expose the branch structure and stability changes that organize local dynamics more transparently. Earlier mathematical studies of Notch signaling already illustrate how tractable reductions can reveal the mechanisms underlying signaling-state selection and pattern formation [21–23]. More broadly, delayed feedback and adaptive regulation are well-known sources of switching and oscillation in biological control circuits [24–28]. These considerations motivate a local bifurcation analysis for density-gated synNotch relay circuits.

We therefore formulate a reduced local model that retains the main ingredients needed for local dynamical analysis: density-gated relay strength, delayed positive activation, cis-inhibition, and slow adaptive inhibition. The adaptive variable is introduced as an effective activity-dependent inhibitory state that summarizes the gradual loss of productive signaling output under sustained crowding and persistent activity. This reduction preserves the two ingredients needed for the dynamics of interest: density-gated changes in equilibrium structure and delay-mediated changes in local stability. At the same time, it is intended as a local closure rather than as a full replacement of the spatial lattice model. Its role is to extract local branch geometry and local stability changes near coherent active patches or locally smooth front segments, not to quantitatively reproduce front speed or spatial pattern morphology in strongly heterogeneous tissues.

The aim of this paper is to determine how density and delay jointly organize the local dynamics of this adaptive synNotch relay. The analysis follows two complementary routes. The first route addresses density-driven saddle-node bifurcation and identifies the conditions under which multiple positive equilibria, bistability, and hysteresis arise. The second route addresses delay-induced Hopf bifurcation and characterizes stability switching and the onset of oscillation around positive equilibria. Numerical calculations guided by the signaling architecture and parameter scales in [14] support both analytical routes and show how density and intracellular processing delay together govern local state selection and rhythmic activity in adaptive synNotch relay circuits. In this sense, the experiments in [14] provide the biological motivation for a reduced model, whereas the present analysis is aimed at local dynamical organization rather than direct quantitative fitting of spatial propagation data.

The paper is organized as follows. Section 2 derives a reduced local model from the lattice framework. Section 3 develops the density-driven fold analysis and the delay-dependent stability theory. Section 4 presents numerical verification, and Section 5 summarizes the main conclusions.

2. Model formulation

We start from the spatial lattice framework in [14]. There, cells occupy a hexagonal lattice, and the incoming ligand signal to a transceiver cell i is

$$I_i(t) = \sum_j w_{ij} s_j(t), \tag{2.1}$$

where $s_j(t)$ is the ligand level on cell j, and $W = (w_{ij})$ is a Gaussian-weighted adjacency matrix normalized by $\sum_j w_{ij} = 1$. This form accounts for contact-dependent signaling together with spatially weighted local interactions.

Our interest here is the local relay dynamics near a coherent active patch or a locally smooth segment of a propagating front. In this setting, the weighted neighborhood input is approximated by an effective local exposure,

$$I_i(t) \approx q\, s(t), \qquad 0 < q \le 1, \tag{2.2}$$

where $s(t)$ denotes a ligand level and q is an effective coupling coefficient determined by local contact geometry. Under this closure, the same variable $s(t)$ represents both the neighborhood input and the ligand level of a transceiver cell.

To indicate the range of validity of (2.2), we write $I_i(t) = q\, s_i(t) + r_i(t)$, with $r_i(t) := \sum_j w_{ij} s_j(t) - q\, s_i(t)$. Then $|r_i(t)| \le \sum_j w_{ij} |s_j(t) - s_i(t)| + |1 - q|\, |s_i(t)|$. The residual is therefore small when neighboring ligand levels vary weakly and q captures the local attenuation of effective contact. The reduced model is intended for this local regime. Near sharp fronts, fragmented clusters, or strongly heterogeneous neighborhoods, the approximation is less accurate and the full lattice description remains necessary.

A second ingredient inherited from [14] is the density-dependent attenuation of synNotch transduction. For the super-confluent regime considered here, we take

$$\beta(\rho) = e^{-m(\rho-1)}, \qquad m > 0, \quad \rho \ge 1, \tag{2.3}$$

so that the effective density-gated trans-activation coupling is

$$B(\rho) = q\beta(\rho) = q\, e^{-m(\rho-1)}. \tag{2.4}$$

To incorporate slower regulatory effects, we introduce an adaptive state $h(t)$ describing the progressive loss of signaling competence under sustained activity. In the present reduced setting, $h(t)$ is an effective inhibitory state. It may represent the combined influence of several slower attenuation mechanisms, such as receptor downregulation, ligand–receptor endocytosis, delayed transcriptional repression, or related activity-dependent feedback processes.

The delay τ acts on the productive activation pathway, so both the activation kernel and the adaptive modulation are evaluated at time $t - \tau$. We define

$$\Phi\big(s(t-\tau);\rho\big) = \frac{\big(B(\rho)s(t-\tau)\big)^p}{k^p + \big(B(\rho)s(t-\tau)\big)^p + \big(\varepsilon s(t-\tau)\big)^p}, \tag{2.5}$$

and obtain the reduced adaptive relay system

$$\begin{cases} \dot{s}(t) = \mu + \dfrac{\alpha}{1 + \chi h(t-\tau)}\, \Phi\big(s(t-\tau);\rho\big) - s(t), \\ \dot{h}(t) = \sigma s(t) - \delta h(t). \end{cases} \tag{2.6}$$

Here, $s(t)$ is the ligand level of a transceiver cell, and $h(t)$ is the adaptive inhibitory state. The parameter α is the maximal induced ligand production rate, k is the inducible promoter threshold, p is the Hill exponent, and ε measures cis-inhibition. The parameter χ sets the strength of adaptive suppression. The parameter σ controls the accumulation rate of the adaptive state, while δ controls its relaxation rate, so that $1/\delta$ is the recovery time scale and the equilibrium relation $h^* = (\sigma/\delta)s^*$ determines the effective adaptive load at steady state. The constant $\mu > 0$ is a small basal leak term. All quantities in Table 1 are nondimensional. Time is scaled by the turnover time of the ligand variable, and the state variables are scaled by reference expression levels.

Table 1. Nondimensional parameter values for the reduced model.

Parameter	Meaning	Value
α	induced ligand production rate	3
k	inducible promoter threshold	0.02
p	promoter cooperativity	2
ε	cis-inhibition strength	1
τ	reference delay used in illustrative computations	0.3
ρ	reference density used in illustrative computations	3
m	density sensitivity of signaling	1
q	effective local exposure factor	1
χ	inhibition strength of adaptive state	1
σ	induction rate of adaptive state	1.3
δ	relaxation rate of adaptive state	0.05
μ	basal ligand leak	10^{-3}

For the delay system (2.6), the state is supplemented with history functions

$$s(\theta) = \varphi_1(\theta), \qquad h(\theta) = \varphi_2(\theta), \qquad \theta \in [-\tau, 0],$$

where $\varphi_1, \varphi_2 \in C([-\tau, 0], \mathbb{R}_+)$ are prescribed nonnegative initial histories. In the numerical simulations, continuous histories are chosen near the equilibrium branch under study.

Figure 1 summarizes the reduced model. A transceiver cell receives an effective neighborhood input described by (2.2). Productive synNotch activation is filtered by the density gate $B(\rho)$ and represented by the delayed kernel $\Phi(s(t-\tau);\rho)$. This activation drives ligand production $s(t)$ and, on a slower time scale, builds up the adaptive state $h(t)$. The feedback factor $(1 + \chi h(t-\tau))^{-1}$ reduces induced ligand production and closes the delayed negative-feedback loop. The resulting system provides a compact local description of density-gated state selection and delay-dependent stability changes in synNotch relay dynamics.

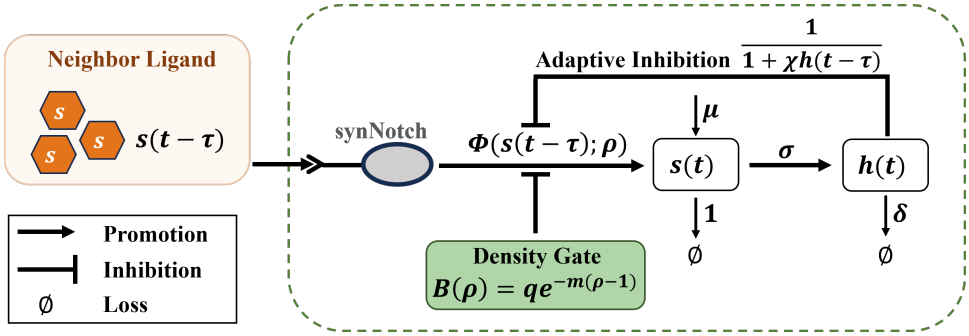

Figure 1. Schematic of the reduced single-cell synNotch transceiver model.

3. Theoretical analysis

The theoretical analysis follows two complementary routes. The first route concerns the equilibrium structure and studies how the density parameter organizes the steady-state branches through saddle-node bifurcation. The second route concerns the local delay-dependent dynamics and studies how intracellular processing delay changes stability and produces oscillatory behavior through Hopf bifurcation. This separation allows the roles of density and delay to be analyzed independently: density determines the multiplicity and geometry of positive equilibria, whereas delay determines whether a selected equilibrium remains stable or develops rhythmic activity.

3.1. Density-driven saddle-node bifurcation

We begin with the equilibrium structure. At any positive equilibrium (s_*, h_*) of system (2.6), the second equation gives

$$h_* = \kappa s_*, \qquad \kappa := \frac{\sigma}{\delta}. \tag{3.1}$$

Introducing

$$\theta := \chi\kappa = \frac{\chi\sigma}{\delta}, \qquad X(\rho) := q^p e^{-mp(\rho-1)}, \tag{3.2}$$

the first equilibrium equation reduces to

$$\mu + \frac{\alpha}{1+\theta s_*}\frac{X(\rho)s_*^p}{k^p + (X(\rho)+\varepsilon^p)s_*^p} - s_* = 0. \tag{3.3}$$

Since the fraction in (3.3) is positive, every positive equilibrium satisfies $s_* > \mu$.

Define

$$A(s) := (s-\mu)(1+\theta s). \tag{3.4}$$

Rearranging (3.3) gives

$$X(\rho) = \frac{A(s)(k^p + \varepsilon^p s^p)}{s^p[\alpha - A(s)]}. \tag{3.5}$$

Hence, positive equilibria are represented by the density–equilibrium map

$$\rho = \mathcal{R}_{\mu,\alpha}(s) := 1 - \frac{1}{mp}\ln\left(\frac{A(s)(k^p + \varepsilon^p s^p)}{q^p s^p[\alpha - A(s)]}\right). \tag{3.6}$$

Its natural domain is

$$\mathcal{D}_\alpha = \{s > \mu : \ A(s) < \alpha\} = (\mu, s_\alpha), \tag{3.7}$$

where $s_\alpha > \mu$ is the unique solution of $A(s) = \alpha$. Indeed,

$$A'(s) = 1 + 2\theta s - \theta\mu > 0, \qquad s > \mu, \tag{3.8}$$

so A is strictly increasing on (μ, ∞).

Theorem 3.1 (Density-driven saddle-node bifurcation and branch stability)**.** *Assume that all parameters in system* (2.6) *are positive.*

(i) Positive equilibria of (2.6) *are in one-to-one correspondence with the roots of*

$$\rho = \mathcal{R}_{\mu,\alpha}(s), \qquad s \in \mathcal{D}_\alpha, \tag{3.9}$$

where

$$\mathcal{R}_{\mu,\alpha}(s) := 1 - \frac{1}{mp} \ln\left(\frac{A(s)(k^p + \varepsilon^p s^p)}{q^p s^p [\alpha - A(s)]}\right), \qquad A(s) := (s - \mu)(1 + \theta s), \tag{3.10}$$

and

$$\mathcal{D}_\alpha = \{s > \mu : \ A(s) < \alpha\} = (\mu, s_\alpha), \tag{3.11}$$

with $s_\alpha > \mu$ being the unique solution of $A(s) = \alpha$.

(ii) The turning points of the equilibrium curve are determined by

$$\mathcal{R}'_{\mu,\alpha}(s) = 0, \tag{3.12}$$

equivalently,

$$\frac{1}{s - \mu} + \frac{\theta}{1 + \theta s} + \frac{p\varepsilon^p s^{p-1}}{k^p + \varepsilon^p s^p} - \frac{p}{s} + \frac{1 + 2\theta s - \theta\mu}{\alpha - (s - \mu)(1 + \theta s)} = 0. \tag{3.13}$$

If $\mathcal{R}_{\mu,\alpha}$ has two distinct nondegenerate critical points

$$\mu < s_-^c < s_+^c < s_\alpha, \qquad \mathcal{R}'_{\mu,\alpha}(s_\pm^c) = 0, \qquad \mathcal{R}''_{\mu,\alpha}(s_\pm^c) \neq 0, \tag{3.14}$$

with

$$\mathcal{R}''_{\mu,\alpha}(s_-^c) > 0, \qquad \mathcal{R}''_{\mu,\alpha}(s_+^c) < 0, \tag{3.15}$$

then the equilibrium curve has a local minimum at s_-^c and a local maximum at s_+^c. Defining

$$\rho_{\text{fold}}^- := \mathcal{R}_{\mu,\alpha}(s_-^c), \qquad \rho_{\text{fold}}^+ := \mathcal{R}_{\mu,\alpha}(s_+^c), \tag{3.16}$$

one obtains a folded equilibrium branch. In particular, if

$$1 \le \rho_{\text{fold}}^- < \rho_{\text{fold}}^+, \tag{3.17}$$

then the biologically admissible regime $\rho \ge 1$ contains one positive equilibrium for $1 \le \rho < \rho_{\text{fold}}^-$, three positive equilibria for $\rho_{\text{fold}}^- < \rho < \rho_{\text{fold}}^+$, and one positive equilibrium for $\rho > \rho_{\text{fold}}^+$.

(iii) Let

$$F(s,\rho) := \mu + \frac{\alpha}{1+\theta s}\frac{q^p e^{-mp(\rho-1)} s^p}{k^p + (q^p e^{-mp(\rho-1)} + \varepsilon^p) s^p} - s. \tag{3.18}$$

At each nondegenerate turning point in (3.14)–(3.15)*, one has*

$$F(s,\rho) = 0, \qquad F_s(s,\rho) = 0, \qquad F_\rho(s,\rho) \neq 0, \qquad F_{ss}(s,\rho) \neq 0. \tag{3.19}$$

Hence each turning point is a simple saddle-node bifurcation point.

(iv) For $\tau = 0$, let (s_*, h_*) be a positive equilibrium and define

$$X_\rho := q^p e^{-mp(\rho-1)}, \qquad D_\rho := k^p + (X_\rho + \varepsilon^p) s_*^p. \tag{3.20}$$

Then, the Jacobian of the non-delayed system is

$$J_0 = \begin{pmatrix} f_s & f_h \\ \sigma & -\delta \end{pmatrix}, \tag{3.21}$$

where

$$f_s = \frac{\alpha p X_\rho k^p s_*^{p-1}}{(1+\chi h_*) D_\rho^2} - 1, \qquad f_h = -\frac{\alpha \chi X_\rho s_*^p}{(1+\chi h_*)^2 D_\rho}. \tag{3.22}$$

Its trace and determinant satisfy

$$\operatorname{tr} J_0(s_*) = \frac{p k^p (s_* - \mu)}{s_* D_\rho} - 1 - \delta, \tag{3.23}$$

and

$$\det J_0(s_*) = \delta\, F_\rho(s_*, \rho)\, \mathcal{R}'_{\mu,\alpha}(s_*), \tag{3.24}$$

with

$$F_\rho(s,\rho) = -\frac{\alpha m p q^p e^{-mp(\rho-1)} s^p (k^p + \varepsilon^p s^p)}{(1+\theta s)\left(k^p + (q^p e^{-mp(\rho-1)} + \varepsilon^p) s^p\right)^2} < 0. \tag{3.25}$$

Therefore, every equilibrium on a branch with $\mathcal{R}'_{\mu,\alpha}(s_*) > 0$ is a saddle, whereas every equilibrium on a branch with $\mathcal{R}'_{\mu,\alpha}(s_*) < 0$ and $\operatorname{tr} J_0(s_*) < 0$ is locally asymptotically stable. In particular, when the two outer branches satisfy $\operatorname{tr} J_0 < 0$, the interval $\rho^-_{\text{fold}} < \rho < \rho^+_{\text{fold}}$ contains low/high bistability.

Proof. Part (i) follows by eliminating h_* through the equilibrium relation $h_* = \kappa s_*$ and rearranging the scalar equilibrium equation into the density–equilibrium map $\rho = \mathcal{R}_{\mu,\alpha}(s)$. The domain $\mathcal{D}_\alpha = (\mu, s_\alpha)$ follows from $s_* > \mu$ and from the strict monotonicity of $A(s) = (s-\mu)(1+\theta s)$ on (μ, ∞).

Part (ii) is obtained by differentiating $\mathcal{R}_{\mu,\alpha}(s)$ with respect to s, which yields (3.13). Moreover,

$$\lim_{s\to\mu^+} \mathcal{R}_{\mu,\alpha}(s) = +\infty, \qquad \lim_{s\to s_\alpha^-} \mathcal{R}_{\mu,\alpha}(s) = -\infty, \tag{3.26}$$

so two nondegenerate critical points with the sign pattern in (3.15) generate the folded equilibrium geometry and the 1–3–1 equilibrium configuration in the biologically admissible range.

For part (iii), equilibria satisfy $F(s,\rho) = 0$. Along the equilibrium branch $\rho = \mathcal{R}_{\mu,\alpha}(s)$,

$$F_s(s, \mathcal{R}_{\mu,\alpha}(s)) + F_\rho(s, \mathcal{R}_{\mu,\alpha}(s)) \mathcal{R}'_{\mu,\alpha}(s) = 0. \tag{3.27}$$

At a turning point, $\mathcal{R}'_{\mu,\alpha}(s) = 0$, hence $F_s = 0$. Since $F_\rho < 0$, differentiating once more gives

$$F_{ss} = -F_\rho \mathcal{R}''_{\mu,\alpha}, \tag{3.28}$$

so $F_{ss} \neq 0$ whenever $\mathcal{R}''_{\mu,\alpha} \neq 0$. This proves that each nondegenerate turning point is a simple fold.

For part (iv), differentiating the non-delayed vector field gives (3.21)–(3.22). Using the equilibrium identity

$$\frac{\alpha X_\rho s_*^p}{(1+\chi h_*)D_\rho} = s_* - \mu, \tag{3.29}$$

one obtains the trace formula (3.23). Since $h = \kappa s$ on the equilibrium manifold,

$$F_s(s_*, \rho) = f_s + \frac{\sigma}{\delta} f_h, \tag{3.30}$$

and, therefore,

$$\det J_0(s_*) = -\delta F_s(s_*, \rho) = \delta\, F_\rho(s_*, \rho)\, \mathcal{R}'_{\mu,\alpha}(s_*). \tag{3.31}$$

Because $F_\rho < 0$, the sign of $\det J_0$ is opposite to the sign of $\mathcal{R}'_{\mu,\alpha}(s_*)$, which gives the branch classification and the stated stability conclusion. □

Theorem 3.1 shows that density organizes the equilibrium structure through a folded branch geometry. When two nondegenerate fold points are present in the biologically admissible regime, the model exhibits a three-equilibrium interval bounded by ρ^-_{fold} and ρ^+_{fold}. At zero delay, the middle branch is always a saddle, whereas the lower and upper outer branches are stable only when the additional trace condition $\operatorname{tr} J_0 < 0$ is satisfied. Thus, the folded geometry identifies the candidate switching region, but actual low/high bistability must be verified from Theorem 3.1(iv) along the outer branches. This folded structure provides the dynamical basis for density-controlled switching and hysteresis.

3.2. Delay-induced Hopf bifurcation

We next study the delay-dependent stability of a positive equilibrium (s_*, h_*) at a fixed admissible density level. Linearizing (2.6) around (s_*, h_*) with

$$u(t) := s(t) - s_*, \qquad v(t) := h(t) - h_*, \tag{3.32}$$

gives

$$\begin{cases} \dot{u}(t) = -u(t) + b\, u(t-\tau) + c\, v(t-\tau), \\ \dot{v}(t) = \sigma u(t) - \delta v(t), \end{cases} \tag{3.33}$$

where

$$b = \frac{\alpha p X_\rho k^p s_*^{p-1}}{(1+\chi h_*)D^2} > 0, \qquad c = -\frac{\alpha\chi X_\rho s_*^p}{(1+\chi h_*)^2 D} = -\frac{\chi(s_* - \mu)}{1+\chi h_*} < 0, \tag{3.34}$$

with

$$X_\rho := q^p e^{-mp(\rho-1)}, \qquad D := k^p + (X_\rho + \varepsilon^p)s_*^p. \tag{3.35}$$

The associated characteristic equation is

$$\Delta(\lambda, \tau) := (\lambda+1)(\lambda+\delta) - (b(\lambda+\delta) - \zeta)e^{-\lambda\tau} = 0, \qquad \zeta := -c\sigma > 0. \tag{3.36}$$

Theorem 3.2 (Delay-induced Hopf criterion)**.** *Let* (s_*, h_*) *be a positive equilibrium of* (2.6)*, and define*

$$G(z) = z^2 + (1 + \delta^2 - b^2)z + \delta^2 - (b\delta - \zeta)^2, \qquad z \geq 0. \tag{3.37}$$

Then, the following statements hold.

(i) The characteristic equation (3.36) *has purely imaginary roots* $\lambda = \pm i\omega$ *with* $\omega > 0$ *if, and only if,* $z = \omega^2$ *is a positive root of* $G(z) = 0$*.*

(ii) If $z_0 > 0$ *is a positive root of* G *and* $\omega_0 = \sqrt{z_0}$*, then the corresponding critical delays are*

$$\tau_n = \frac{1}{\omega_0}\Big[\operatorname{atan2}(b\omega_0,\ b\delta - \zeta) - \operatorname{atan2}((1+\delta)\omega_0,\ \delta - \omega_0^2) + 2n\pi\Big], \qquad n \in \mathbb{N}_0. \tag{3.38}$$

(iii) If z_0 *is a simple positive root of* G*, then the corresponding root pair satisfies*

$$\operatorname{sgn}\left[\Re\left(\frac{d\lambda}{d\tau}\right)\Big|_{\lambda=i\omega_0,\ \tau=\tau_n}\right] = \operatorname{sgn}(G'(z_0)) \neq 0. \tag{3.39}$$

Hence, the sign of $G'(z_0)$ *determines the crossing direction. If, in addition, no other characteristic roots lie on the imaginary axis at* $\tau = \tau_n$*, then* (2.6) *undergoes a local Hopf bifurcation at* $\tau = \tau_n$*.*

Proof. Substituting $\lambda = i\omega$ into (3.36) gives

$$(i\omega + 1)(i\omega + \delta) = (ib\omega + b\delta - \zeta)e^{-i\omega\tau}. \tag{3.40}$$

Taking moduli yields

$$(\omega^2 + 1)(\omega^2 + \delta^2) = (b\delta - \zeta)^2 + b^2\omega^2, \tag{3.41}$$

which is equivalent to $G(\omega^2) = 0$. This proves part (i).

For part (ii), write

$$P(i\omega_0) = (i\omega_0 + 1)(i\omega_0 + \delta), \qquad Q(i\omega_0) = ib\omega_0 + b\delta - \zeta. \tag{3.42}$$

Then, (3.40) implies

$$P(i\omega_0) = Q(i\omega_0)e^{-i\omega_0\tau}, \tag{3.43}$$

so the phase balance gives (3.38).

For part (iii), differentiating (3.36) implicitly with respect to τ and evaluating at $\lambda = i\omega_0$ gives

$$\Re\left[\left(\frac{d\lambda}{d\tau}\right)^{-1}\right] = \frac{G'(\omega_0^2)}{|P(i\omega_0)|^2}. \tag{3.44}$$

Since $|P(i\omega_0)|^2 > 0$, the sign of $\Re(d\lambda/d\tau)$ is the sign of $G'(\omega_0^2)$, which proves the transversality statement. □

A useful sufficient condition for the existence of a positive root of G is

$$G(0) = \delta^2 - (b\delta - \zeta)^2 < 0. \tag{3.45}$$

Since G is a quadratic polynomial in $z = \omega^2$, (3.41) can yield no positive Hopf frequency, one positive Hopf frequency, or two positive Hopf frequencies. Thus, the delay system has at most two distinct positive frequencies associated with purely imaginary characteristic roots. Indeed, if (3.45) holds, then $G(0) < 0$ and $G(z) \to +\infty$ as $z \to +\infty$, so G has at least one positive root.

The Hopf route complements the equilibrium analysis in a precise way. Density selects the available positive equilibria and determines whether bistability is possible, whereas delay governs the spectrum near a chosen equilibrium. When the polynomial G has one or more positive roots, the corresponding critical delays locate stability switches. If several positive roots are present, the associated crossings may play different dynamical roles, and the sign of $G'(z_0)$ identifies whether a given delay crossing stabilizes or destabilizes the equilibrium.

The stabilization effect can be interpreted directly from the characteristic equation $\Delta(\lambda, \tau) = (\lambda + 1)(\lambda + \delta) - (b(\lambda + \delta) - \zeta)e^{-\lambda\tau} = 0$, where $b > 0$ describes delayed positive relay, $c < 0$ describes delayed adaptive inhibition, and $\zeta = -c\sigma > 0$ is the effective strength of the delayed adaptive channel. Because the delayed term contains the combination $b(\lambda + \delta) - \zeta$, the delay acts through two competing components rather than through a single positive feedback loop. The positive relay term tends to promote instability, whereas the adaptive contribution partially offsets it.

This competition is reflected in the auxiliary polynomial $G(z) = z^2 + (1 + \delta^2 - b^2)z + \delta^2 - (b\delta - \zeta)^2$. When G has two positive roots $z_1 < z_2$, the smaller root may satisfy $G'(z_1) < 0$ while the larger root satisfies $G'(z_2) > 0$. In that case, the first delay crossing is stabilizing and the second is destabilizing. Thus, delay-induced stabilization is possible when the delayed positive relay is strong enough to make the zero-delay equilibrium unstable, but the delayed adaptive inhibition is also strong enough to reverse the first crossing direction at low frequency. This mechanism depends on the relative magnitudes of b, δ, and ζ, and therefore occurs only in a restricted parameter regime rather than universally.

4. Numerical simulation

4.1. Density-driven saddle-node bifurcation

We first verify the density-driven branch structure predicted by Theorem 3.1. Using the parameter values in Table 1, we obtain $\kappa = \frac{\sigma}{\delta} = 26$ and $\theta = \chi\kappa = 26$. The admissible interval of the equilibrium map is determined by the unique solution of $(s - \mu)(1 + \theta s) = \alpha$, which gives $s_\alpha \approx 0.3215$. Solving $\mathcal{R}'_{\mu,\alpha}(s) = 0$ yields two turning points, $s_c^- \approx 0.0021$ and $s_c^+ \approx 0.0139$, with corresponding fold densities $\rho_{\text{fold}}^- \approx 2.6694$ and $\rho_{\text{fold}}^+ \approx 3.0065$. Moreover, $\mathcal{R}''_{\mu,\alpha}(s_c^-) \approx 1.9743 \times 10^5 > 0$ and $\mathcal{R}''_{\mu,\alpha}(s_c^+) \approx -2.5983 \times 10^3 < 0$, so both turning points are nondegenerate, in agreement with the saddle-node conditions in Theorem 3.1.

Figure 2(a) displays the equilibrium map $\rho = \mathcal{R}_{\mu,\alpha}(s)$. The branch attains a local minimum at $\text{SN}_1 = (\rho_{\text{fold}}^-, \text{s}_\text{c}^-)$ and a local maximum at $\text{SN}_2 = (\rho_{\text{fold}}^+, \text{s}_\text{c}^+)$. Hence, the interval $(\rho_{\text{fold}}^-, \rho_{\text{fold}}^+) \approx (2.6694, 3.0065)$ is precisely the density range in which three positive equilibria coexist, whereas only one positive equilibrium remains outside this interval. This reproduces the 1–3–1 equilibrium configuration predicted by the equilibrium map.

Figure 2(b) shows the corresponding static bifurcation diagram together with the zero-trace point on the upper branch. The continuation confirms the folded three-branch geometry: the middle branch is unstable and connects the two fold points, while the lower branch remains stable throughout the plotted range. However, the upper branch is not stable on the entire three-equilibrium interval. A numerical

evaluation of $\operatorname{tr} J_0$ along the upper branch yields a zero crossing at $\rho_{\mathrm{tr}}^{+} \approx 2.9908$, marked by TR_{+} in Figure 2(b). Therefore, the upper branch is stable only for $\rho_{\mathrm{fold}}^{-} < \rho < \rho_{\mathrm{tr}}^{+}$, and becomes unstable for $\rho_{\mathrm{tr}}^{+} < \rho < \rho_{\mathrm{fold}}^{+}$, before terminating at the upper fold SN_2. Consequently, the genuine low/high bistable interval at $\tau = 0$ is not the full three-equilibrium window, but only $(\rho_{\mathrm{fold}}^{-}, \rho_{\mathrm{tr}}^{+}) \approx (2.6694, 2.9908)$.

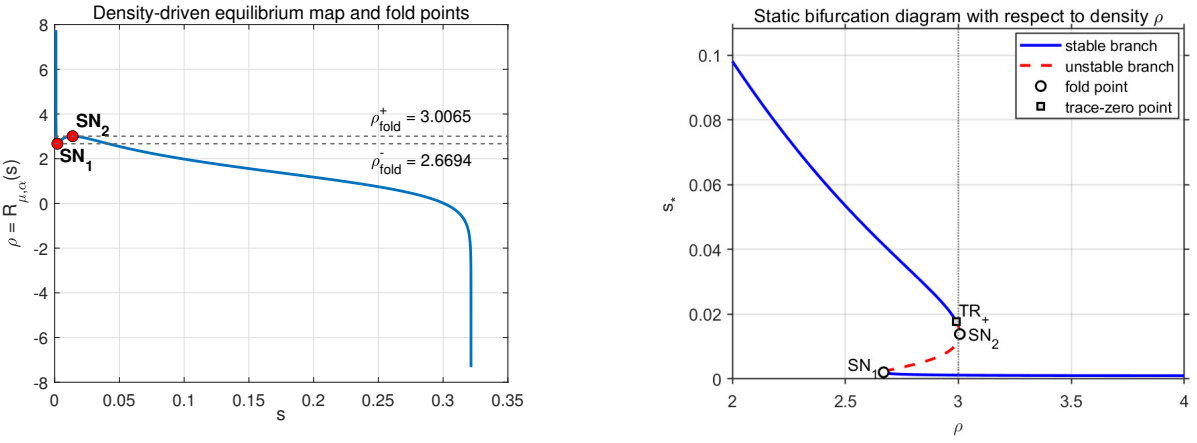

(a) **(b)**

Figure 2. Numerical verification of the density-driven fold structure. (a) Density-driven equilibrium map $\rho = \mathcal{R}_{\mu,\alpha}(s)$ with fold points SN_1 and SN_2. (b) Static bifurcation diagram with respect to ρ, showing the folded three-branch structure and the trace-zero point on the upper branch.

4.2. Delay-induced Hopf bifurcation

We next examine the delay-dependent dynamics at $\rho = 3$. This value lies inside the three-equilibrium window $(\rho_{\mathrm{fold}}^{-}, \rho_{\mathrm{fold}}^{+}) \approx (2.6694, 3.0065)$. A numerical evaluation of $\operatorname{tr} J_0$ along the upper branch yields a zero crossing at $\rho_{\mathrm{tr}}^{+} \approx 2.9908$, so the genuine low/high bistable interval at $\tau = 0$ is only $(\rho_{\mathrm{fold}}^{-}, \rho_{\mathrm{tr}}^{+}) \approx (2.6694, 2.9908)$. Therefore, although three positive equilibria still coexist at $\rho = 3$, the upper equilibrium considered here is already unstable in the non-delayed problem. For the parameter set in Table 1, the steady states are $E_1 = (s_1, h_1) \approx (0.0012, 0.0309)$, $E_2 = (s_2, h_2) \approx (0.0118, 0.3057)$, and $E_3 = (s_3, h_3) \approx (0.0162, 0.4223)$. The Jacobian of the non-delayed system shows that E_1 is locally asymptotically stable, E_2 is a saddle, and E_3 is unstable at $\tau = 0$.

The delay-induced transition occurs on the upper equilibrium branch. For E_3, the auxiliary polynomial G has two positive roots, $z_1 \approx 0.0028$ and $z_2 \approx 0.2553$, which correspond to the critical delays $\tau_0^{(1)} \approx 1.63$ and $\tau_0^{(2)} \approx 11.56$. The signs $G'(z_1) < 0$ and $G'(z_2) > 0$ indicate that the first crossing stabilizes E_3, whereas the second crossing destabilizes it. Hence, the characteristic-equation analysis predicts the following delay-dependent stability switching on the upper branch: E_3 is unstable for $0 \le \tau < \tau_0^{(1)}$, stable for $\tau_0^{(1)} < \tau < \tau_0^{(2)}$, and unstable again for $\tau > \tau_0^{(2)}$. Beyond the second threshold, the loss of stability is accompanied by the emergence of a stable oscillatory response.

Figure 3 provides numerical verification of this scenario. In Figure 3(a), we plot the delay-induced bifurcation diagram on the upper equilibrium branch E_3 with τ as the control parameter. The horizontal branch corresponds to the equilibrium level $s = s_3$, shown as unstable for $\tau < \tau_0^{(1)}$, stable for $\tau_0^{(1)} < \tau < \tau_0^{(2)}$, and unstable again for $\tau > \tau_0^{(2)}$. The two critical delays $\tau_0^{(1)} \approx 1.63$ and $\tau_0^{(2)} \approx 11.56$ are marked

on the branch. For $\tau > \tau_0^{(2)}$, the green curves show the numerically computed extrema of the periodic orbit, indicating the emergence of a nontrivial oscillatory branch after the second Hopf crossing.

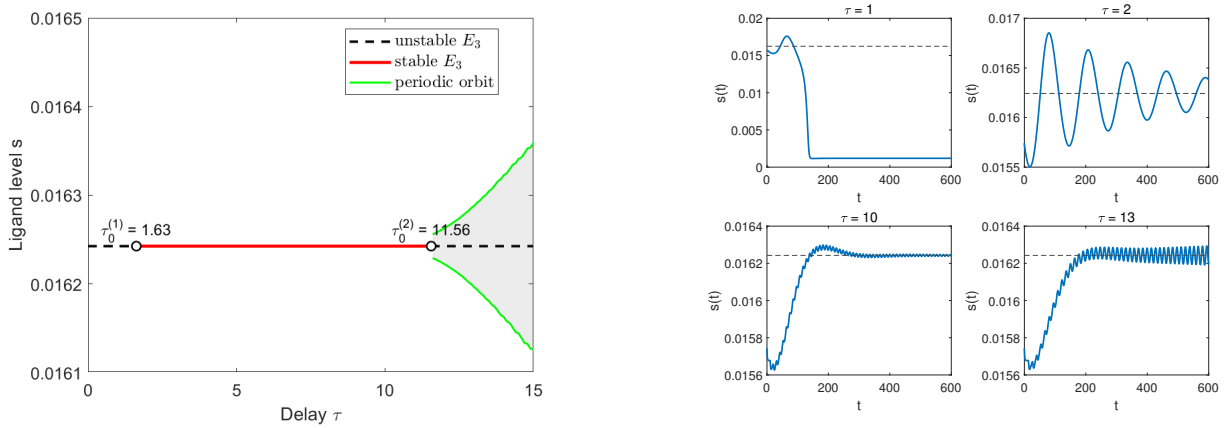

(a) **(b)**

Figure 3. Numerical verification of the delay-induced Hopf bifurcation. (a) Delay-induced Hopf bifurcation diagram on the upper equilibrium branch E_3 with τ as the bifurcation parameter. (b) Time series of $s(t)$ for representative delay values.

The time series in Figure 3(b) further illustrate the stability switching predicted by Theorem 3.2. At $\tau = 1 < \tau_0^{(1)}$, trajectories initiated near the upper branch do not remain close to E_3 and instead leave the upper state, indicating that E_3 is unstable in the small-delay regime. At $\tau = 2$, which lies just above the first threshold, the solution exhibits damped oscillations and relaxes toward the constant level s_3, confirming the delay-induced stabilization of E_3. The same convergent behavior is observed more clearly at $\tau = 10$, where the trajectory approaches the upper equilibrium after a transient stage. In contrast, at $\tau = 13 > \tau_0^{(2)}$, the oscillation amplitude remains bounded away from zero after the transient, indicating convergence to a stable periodic orbit. These simulations therefore agree with the two-crossing Hopf picture obtained from the characteristic equation: the first critical delay stabilizes the upper equilibrium, whereas the second destabilizes it and gives rise to sustained oscillation.

From the viewpoint of practical relevance, the baseline reference delay in Table 1, $\tau = 0.3$, is much smaller than the first critical delay $\tau_0^{(1)} \approx 1.63$ at $\rho = 3$. Therefore the baseline parameter set does not predict oscillation for the nominal delay used in the illustrative computations. Instead, the Hopf analysis identifies a delayed regime that becomes accessible only when the effective delay is sufficiently enlarged. In this sense, the oscillatory behavior in Figure 3 can be interpreted as a dynamical possibility of the reduced model rather than as a direct quantitative prediction for the reference synNotch experiments.

The present reduced model is consistent with the experimental setting of [14] at the level of mechanism: density enters through the effective relay factor $B(\rho) = qe^{-m(\rho-1)}$, and delayed intracellular processing enters through the lag τ in the productive activation pathway. These two ingredients reflect the experimentally observed roles of crowding and response timing in synNotch relay behavior. At the same time, the current model is local and does not explicitly resolve tissue growth, front motion, or spatial contact heterogeneity. Therefore, quantities such as signal propagation speed or full spatial response curves cannot be compared directly with the present two-dimensional reduction. The fold

and Hopf thresholds derived here should instead be interpreted as local organizing thresholds that help explain how density and delay may bias state selection and local temporal response within the broader spatial framework.

4.3. Sensitivity of the Hopf thresholds

To examine how key parameters shift the two Hopf thresholds on the upper equilibrium branch, we perform a one-at-a-time sensitivity analysis at $\rho = 3$. Starting from the baseline parameter set in Table 1, we vary one parameter at a time while keeping all others fixed, and recompute the two Hopf thresholds determined by Theorem 3.2. The four parameters considered here are the adaptive inhibition strength χ, the induction rate σ, the relaxation rate δ, and the density sensitivity coefficient m.

Figure 4 shows that, within the displayed parameter neighborhoods around the baseline values, the two critical delays respond in a systematic but opposite manner. As χ increases, the first critical delay $\tau_0^{(1)}$ increases whereas the second critical delay $\tau_0^{(2)}$ decreases. The same qualitative trend is observed when σ increases. By contrast, increasing δ decreases $\tau_0^{(1)}$ and increases $\tau_0^{(2)}$. A similar opposite trend is also observed for m: larger m shifts $\tau_0^{(1)}$ upward and $\tau_0^{(2)}$ downward. Hence, in the baseline regime considered here, larger χ, σ, or m compress the intermediate stable-delay window $(\tau_0^{(1)}, \tau_0^{(2)})$, whereas larger δ expands it.

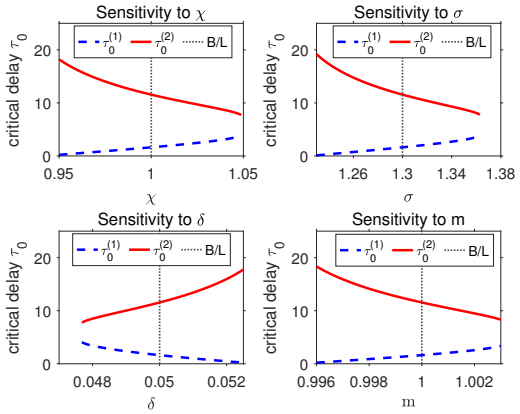

Figure 4. Sensitivity analysis of the Hopf thresholds on the upper equilibrium branch E_3 at $\rho = 3$. Each panel shows the dependence of the stabilizing threshold $\tau_0^{(1)}$ and the destabilizing threshold $\tau_0^{(2)}$ on one parameter, with all other parameters fixed at the baseline values in Table 1. The dashed black line marks the baseline value used in the main simulations, and the abbreviation B/L denotes the baseline value.

These trends are consistent with the feedback structure of the reduced model. The sensitivity curves should be interpreted as local model-based trends, since the parameters describe effective feedback strength and time scales rather than directly measured molecular constants. Figure 4 therefore serves as a qualitative robustness check of the Hopf scenario and indicates how adaptive inhibition and density attenuation may shift the oscillatory regime in the reduced system.

5. Conclusions

This paper proposed a reduced synNotch relay model to study how local density and intracellular processing delay shape signaling dynamics. The model incorporates density-dependent attenuation, delayed positive relay, cis-inhibition, and a slow adaptive inhibitory effect in a compact local framework. Within this setting, the analysis follows two complementary routes. The first concerns density-driven saddle-node bifurcation and identifies how variation in density organizes the equilibrium branches, produces a folded branch structure, and generates a three-equilibrium interval together with a low/high bistable subinterval when the outer-branch trace condition is satisfied. The second concerns delay-induced Hopf bifurcation and determines how delay changes the local stability of positive equilibria through stability switching, including the onset of periodic oscillation on the upper branch.

The numerical results support both parts of the analysis. Continuation of the equilibrium map recovers the folded branch geometry and shows that, for the chosen parameter set, the bistable subinterval ends before the upper fold because the upper branch loses stability at a trace-zero point. Delay computations then verify the two-crossing Hopf scenario on the upper equilibrium branch: the first critical delay stabilizes the equilibrium, and the second destabilizes it and is followed numerically by a periodic branch. The sensitivity analysis further shows that the two Hopf thresholds vary systematically with the adaptive feedback parameters and the density sensitivity coefficient, which clarifies how the stable-delay window shifts in the reduced system.

Taken together, these results provide a local dynamical description of state selection and delay-dependent stability in adaptive synNotch relay circuits. Density determines the available equilibrium states and the range of genuine bistability, while delay determines whether the selected high-signaling state remains stationary or develops oscillatory behavior. For the baseline parameter set considered here, the nominal reference delay remains below the Hopf thresholds on the upper branch. The oscillatory regime should therefore be interpreted as a delayed-feedback scenario admitted by the reduced model under sufficiently large effective delays or altered feedback parameters, rather than as a calibrated prediction for the reference experimental setting.

Two extensions are particularly important. One is to reconnect the local reduction to the full spatial lattice framework and determine how contact heterogeneity and front steepness shift the fold and Hopf thresholds in heterogeneous tissues. The other is to calibrate the reduced dynamics against measured temporal response data and to compare alternative forms of adaptive inhibition. These steps would clarify how the local thresholds identified here relate to multicellular synNotch patterning and experimentally accessible regimes.

Author contributions

Huichao Xing: Investigation, software, writing – original draft, writing – review & editing. Jun Wu: Formal analysis, visualization, writing – review & editing. Conghua Wang: Conceptualization, funding acquisition, project administration, methodology, writing – review & editing. All authors have read and approved the final version of the manuscript for publication.

Use of Generative-AI tools declaration

The authors declare they have not used Artificial Intelligence (AI) tools in the creation of this article.

Acknowledgments

This work was supported in part by the Natural Science Foundation of Chongqing (CSTB2025NSCQ-GPX1007) and the Science and Technology Research Program of Chongqing Municipal Education Commission (KJQN202500505).

Conflict of interest

All authors declare no conflicts of interest in this paper.

References

1. S. Toda, J. M. Brunger, W. A. Lim, Synthetic development: learning to program multicellular self-organization, *Curr. Opin. Syst. Biol.*, **14** (2019), 41–49. https://doi.org/10.1016/j.coisb.2019.02.008
2. J. Davies, M. Levin, Synthetic morphology with agential materials, *Nat. Rev. Bioeng.*, **1** (2023), 46–59. https://doi.org/10.1038/s44222-022-00001-9
3. T. P. Padial, S. Chen, A. C. Hortelão, A. Sen, S. Sánchez, Swarming intelligence in self-propelled micromotors and nanomotors, *Nat. Rev. Mater.*, **10** (2025), 947–963. https://doi.org/10.1038/s41578-025-00818-x
4. L. Morsut, K. T. Roybal, X. Xiong, R. M. Gordley, S. M. Coyle, M. Thomson, et al., Engineering customized cell sensing and response behaviors using synthetic Notch receptors, *Cell*, **164** (2016), 780–791. https://doi.org/10.1016/j.cell.2016.01.012
5. K. T. Roybal, L. J. Rupp, L. Morsut, W. J. Walker, K. A. McNally, J. S. Park, et al., Precision tumor recognition by T cells with combinatorial antigen-sensing circuits, *Cell*, **164** (2016), 770–779. https://doi.org/10.1016/j.cell.2016.01.011
6. F. Teng, T. Cui, L. Zhou, Q. Gao, Q. Zhou, W. Li, Programmable synthetic receptors: the next-generation of cell and gene therapies, *Sig. Transduct. Target. Ther.*, **9** (2024), 7. https://doi.org/10.1038/s41392-023-01680-5
7. D. Chen, X. Liu, H. Wang, R. M. Merks, D. A. Baker, A model of Notch signalling control of angiogenesis: Evidence of a role for Notch ligand heterodimerization, *PLoS Comput. Biol.*, **21** (2025), e1012825. https://doi.org/10.1371/journal.pcbi.1012825
8. S. J. Bray, A. Bigas, Modes of Notch signalling in development and disease, *Nat. Rev. Mol. Cell Biol.*, **26** (2025), 522–537. https://doi.org/10.1038/s41580-025-00835-2
9. D. Sprinzak, A. Lakhanpal, L. LeBon, L. A. Santat, M. E. Fontes, G. A. Anderson, et al., Cis-interactions between Notch and Delta generate mutually exclusive signalling states, *Nature*, **465** (2010), 86–90. https://doi.org/10.1038/nature08959

10. L. Tveriakhina, G. Scanavachi, E. D. Egan, R. B. D. C. Correia, A. P. Martin, J. M. Rogers, et al., Temporal dynamics and stoichiometry in human Notch signaling from Notch synaptic complex formation to nuclear entry of the Notch intracellular domain, *Dev. Cell*, **59** (2024), 1425–1438. https://doi.org/10.1016/j.devcel.2024.03.021

11. H. Moghimianavval, C. Newell, P. Parvizian, M. J. Booth, A. P. Liu, Strategies and applications of synthetic cell communication, *Nat. Chem. Biol.*, **21** (2025), 1317–1329. https://doi.org/10.1038/s41589-025-02002-2

12. A. Burgstaller, S. Madureira, O. Staufer, Synthetic cells in tissue engineering, *Curr. Opin. Biotechnol.*, **92** (2025), 103252. https://doi.org/10.1016/j.copbio.2024.103252

13. H. Momiji, K. L. Hassall, K. Featherstone, A. V. McNamara, A. L. Patist, D. G. Spiller, et al., Disentangling juxtacrine from paracrine signalling in dynamic tissue, *PLoS Comput. Biol.*, **15** (2019), e1007030. https://doi.org/10.1371/journal.pcbi.1007030

14. M. Santorelli, P. S. Bhamidipati, J. Courte, B. Swedlund, N. Jain, K. Poon, et al., Control of spatio-temporal patterning via cell growth in a multicellular synthetic gene circuit, *Nat. Commun.*, **15** (2024), 9867. https://doi.org/10.1038/s41467-024-53078-8

15. J. E. Dawson, A. Bryant, B. Walton, S. Bhikot, S. Macon, A. Ajamu-Johnson, et al., Contact area and tissue growth dynamics shape synthetic juxtacrine signaling patterns, *Biophys. J.*, **124** (2025), 93–106. https://doi.org/10.1016/j.bpj.2024.11.007

16. M. Garibyan, T. Hoffman, T. Makaske, S. K. Do, Y. Wu, B. A. Williams, et al., Engineering programmable material-to-cell pathways via synthetic notch receptors to spatially control differentiation in multicellular constructs, *Nat. Commun.*, **15** (2024), 5891. https://doi.org/10.1038/s41467-024-50126-1

17. Y. Nie, Z. Yang, T. Huang, C. Wang, Dynamic analysis and robust strategy for the delayed paradoxical cell population control circuit, *IEEE Trans. Cybern.*, **55** (2025), 2719–2728. https://doi.org/10.1109/TCYB.2025.3556585

18. C. Wang, Y. Zhang, J. Cao, Z. Yang, Oscillatory dynamics and regulatory mechanisms of the p53–Per2 network in DNA-damaged cells, *IEEE Trans. Neural Networks Learn. Syst.*, **36** (2025), 9725–9732. https://doi.org/10.1109/TNNLS.2024.3424784

19. Z. Wang, B. Hu, L. Zhu, J. Lin, M. Xu, D. Wang, Hopf bifurcation analysis for Parkinson oscillation with heterogeneous delays: A theoretical derivation and simulation analysis, *Commun. Nonlinear Sci. Numer. Simul.*, **114** (2022), 106614. https://doi.org/10.1016/j.cnsns.2022.106614

20. T. Gao, X. Meng, Stability and Hopf bifurcation of a delayed diffusive phytoplankton-zooplankton-fish model with refuge and two functional responses, *AIMS Math.*, **8** (2023), 8867–8901. https://doi.org/10.3934/math.2023445

21. T. Troost, U. Binshtok, D. Sprinzak, T. Klein, Cis-inhibition suppresses basal Notch signaling during sensory organ precursor selection, *Proc. Natl. Acad. Sci. U.S.A.*, **120** (2023), e2214535120. https://doi.org/10.1073/pnas.2214535120

22. D. Chen, Z. Forghany, X. Liu, H. Wang, R. M. Merks, D. A. Baker, A new model of Notch signalling: Control of Notch receptor cis-inhibition via Notch ligand dimers, *PLoS Comput. Biol.*, **19** (2023), e1010169. https://doi.org/10.1371/journal.pcbi.1010169

23. Y. Zhang, J. Cao, L. Liu, H. Liu, Z. Li, Complex role of time delay in dynamical coordination of neural progenitor fate decisions mediated by Notch pathway, *Chaos Soliton Fract.*, **180** (2024), 114479. https://doi.org/10.1016/j.chaos.2024.114479

24. Y. Wang, A. Zeb, R. K. Upadhyay, A. Pratap, A delayed synthetic drug transmission model with two stages of addiction and Holling Type-II functional response, *AIMS Math.*, **6** (2021), 1–22. https://doi.org/10.3934/math.2021001

25. L. Hua, J. Sun, W. Li, Y. Pang, Oscillation of solutions for second-order neutral multi-delay differential equations, *AIMS Math.*, **10** (2025), 18586–18602. https://doi.org/10.3934/math.2025830

26. Z. Wang, B. Hu, W. Zhou, M. Xu, D. Wang, Hopf bifurcation mechanism analysis in an improved cortex-basal ganglia network with distributed delays: An application to Parkinson's disease, *Chaos Soliton Fract.*, **166** (2023), 113022. https://doi.org/10.1016/j.chaos.2022.113022

27. J. G. Wang, X. Y. Meng, X. Lei, Bifurcations and control of plant–herbivore systems with spatiotemporal nonlocal effects in arid regions, *Int. J. Bifurcat. Chaos*, **36** (2026), 2650071. https://doi.org/10.1142/S0218127426500719

28. X. Y. Meng, Z. W. Liang, Dynamics analysis of a delayed diffusive predator–prey model with memory-based diffusion and fear effect of prey, *Int. J. Biomath.*, 2025, 2550101. https://doi.org/10.1142/S1793524525501013

AIMS Press